

Quantum-enhanced sensing from non-Hermitian topology

Saubhik Sarkar,^{1,*} Francesco Ciccarello,^{2,3,†} Angelo Carollo,^{2,‡} and Abolfazl Bayat^{1,4,§}

¹*Institute of Fundamental and Frontier Sciences, University of Electronic Science and Technology of China, Chengdu 610051, China*

²*Universit'a degli Studi di Palermo, Dipartimento di Fisica e Chimica – Emilio Segr'e, via Archirafi 36, I-90123 Palermo, Italy*

³*NEST, Istituto Nanoscienze-CNR, Piazza S. Silvestro 12, 56127 Pisa, Italy*

⁴*Key Laboratory of Quantum Physics and Photonic Quantum Information, Ministry of Education, University of Electronic Science and Technology of China, Chengdu 611731, China*

Non-Hermitian physics predicts open quantum system dynamics with unique topological features such as exceptional points and the non-Hermitian skin effect. We show that this new paradigm of topological systems can serve as probes for bulk Hamiltonian parameters with quantum-enhanced sensitivity reaching Heisenberg scaling. Such enhancement occurs close to a spectral topological phase transition, where the entire spectrum undergoes a delocalization transition. We provide an explanation for this enhanced sensitivity based on the closing of point gap, which is a genuinely non-Hermitian energy gap with no Hermitian counterpart. This establishes a direct connection between energy-gap closing and quantum enhancement in the non-Hermitian realm. Our findings are demonstrated through several paradigmatic non-Hermitian topological models in various dimensions and potential experimental implementations.

Introduction.— Non-Hermitian (NH) Hamiltonians are a longstanding tool for describing open system dynamics. Nonetheless, only in recent years it was realized that NH systems can exhibit fundamentally new phenomena in both classical and quantum systems with topological nature [1]. These include the occurrence of exceptional points, the NH skin effect and violation of bulk-boundary correspondence [2, 3]. Such effects stem from the unique topology caused by energy gaps in the complex spectrum of NH systems, which can be of two different types: the line gap and the point gap [4]. A line gap is a reference line in the complex energy plane that separates different bands, see Fig. 1(a). On the other hand, a point gap is a reference energy that is not reachable by any eigenstates of the NH Hamiltonian, see Fig. 1(b). When the spectrum forms a loop, any interior point is a point gap with non-trivial spectral topology. In this case, the topological invariant is the nonzero spectral winding number [4].

A major feature of NH physics is the extreme sensitivity of the spectrum to boundary conditions, e.g. the coupling at the boundary that can smoothly change from Open Boundary Conditions (OBC) to Periodic Boundary Conditions (PBC). This phenomenon has been exploited for quantum-enhanced sensing protocols with NH probes to estimate the coupling at the boundary [5–19]. In contrast, the *bulk* Hamiltonian parameter estimation problem is hardly explored. Most topological features are associated with the boundary and the conventional bulk-boundary correspondence breaks down in the presence of NH skin effect. The capability of such systems for detecting bulk parameters is therefore nontrivial and can provide new insight into the origin of quantum-enhanced sensitivity. Devising such quantum sensors based on NH topology is highly desirable as this would advance quantum sensing in the presence of decoherence.

In general, a sensing protocol aims to enhance the accuracy in the estimation of an unknown parameter λ , which is encoded in the state of a (classical or quantum) system called *probe*. Accuracy is quantified by the statistical standard deviation $\delta\lambda$, which is lower-bounded according to the

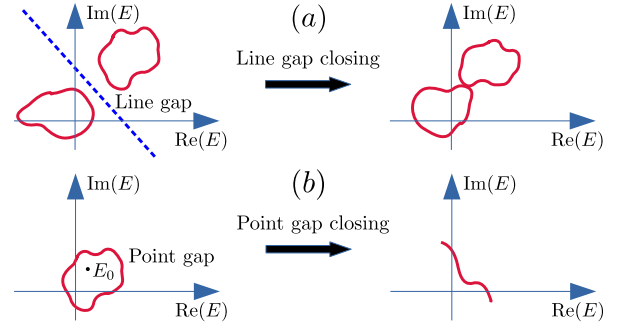


FIG. 1. Energy gaps of NH Hamiltonians in complex energy plane. (a) Line gap (blue dashed line) separating two NH bands (red loops). Line gap closes when the loops merge. (b) Point gap inside a spectral loop (e.g. E_0). Point gap closes when the loop shrinks to an arc.

well-known Cramér-Rao inequality, $\delta\lambda \geq 1/\sqrt{\mathcal{M}F}$. Here, \mathcal{M} is the number of independent trials and F is the Fisher information [20], which in general grows with the probe size L as $F \sim L^b$ with a positive exponent b . The maximal scaling achievable with a classical probe is $b=1$ (standard limit). Using a quantum probe, instead, can result in $b>1$. Such quantum-enhanced sensitivity typically exploits genuine quantum features such as superposition and entanglement. For instance, using Greenberger-Horne-Zeilinger entangled states one can achieve $b=2$ (Heisenberg limit) [21–25]. However, these probes may suffer from extreme detrimental effects in the presence of decoherence [26] or perturbations in the system [27]. These problems can be tackled using quantum many-body sensors, while still achieving enhanced sensitivity near quantum criticality. This was shown for various types of quantum phase transitions such as second-order [28–38], Floquet [39, 40], Stark-localization [41, 42], boundary time crystal [43, 44], and topological [45] phase transitions. All of these transitions bear one common feature, which is the closing of an energy gap. Accordingly, it is natural to conjecture that *energy-gap closing* is the fundamental ingredient for quantum enhancement. Therefore, it is conceptually im-

portant to assess the possibility of enhanced sensitivity in NH systems due to their unique energy gaps (see Fig. 1) that have no correspondence in Hermitian systems.

In this work, we show that NH topological systems can indeed achieve quantum-enhanced sensitivity with Heisenberg scaling as a direct consequence of point gap closing (see Fig. 1(b)). Our results are established through the study of several prototypical NH topological systems in various dimensions and even with disorder. We also point out how this enhancement can be observed in ongoing experiments.

Parameter estimation.— To estimate a single unknown parameter λ , this is first encoded in a probe's quantum state ρ_λ . Next, a measurement on the system is performed, the outcomes of which are processed by a statistical estimation algorithm. The measurement is described by a set of projective operators $\{\Pi_n\}$ with the probability of the n th outcome given by $p_n(\lambda) = \text{Tr}[\rho_\lambda \Pi_n]$. With this classical probability distribution, the lower bound of accuracy is associated with the basis-dependent classical Fisher information, $F_C = \sum_n p_n (\partial_\lambda \log p_n)^2$ [20]. The maximum of F_C over all possible measurements is called the quantum Fisher information (QFI), which achieves the ultimate precision bound. QFI can be expressed as $F_Q = \text{Tr}[\mathcal{L}_\lambda^2 \rho_\lambda]$, with the symmetric logarithmic derivative operator \mathcal{L}_λ defined implicitly as $\partial_\lambda \rho_\lambda = (\rho_\lambda \mathcal{L}_\lambda + \mathcal{L}_\lambda \rho_\lambda)/2$. For pure states $\rho_\lambda = |\psi_\lambda\rangle\langle\psi_\lambda|$ one gets $\mathcal{L}_\lambda = 2\partial_\lambda \rho_\lambda$, and hence $F_Q = 4(\langle\partial_\lambda \psi_\lambda|\partial_\lambda \psi_\lambda\rangle - |\langle\partial_\lambda \psi_\lambda|\psi_\lambda\rangle|^2)$ [20]. While the optimal measurement basis to obtain the ultimate precision bound is not unique, one choice is always given by the \mathcal{L}_λ eigenbasis.

Spectral topology and NH skin effect.— In Hermitian systems, topological phase transitions are accompanied by a band gap closing under PBC and correspond to the emergence of gapless edge states under OBC [46]. The Hermitian band gap closing is topologically equivalent to the line gap closing in NH systems [4] [see Fig. 1(a)]. This suggests that quantum-enhanced sensitivity can also be achieved near a NH line gap closure. However, NH systems also support a unique topology of the complex spectra, which has no correspondence in Hermitian systems. In 1D lattice systems with PBC, the spectra can form loops due to the cyclic nature of the quasi-momentum. Point gaps in the interior of these loops (see Fig. 1(b)) are associated to a non-zero spectral winding number [4]. Presence of a spectral loop corresponds to NH skin effect, i.e. edge-localization of all bulk eigenstates under OBC [47]. When the Hamiltonian parameters are varied in a way that the PBC loops contract to arcs, the NH skin effect vanishes [48, 49]. We refer to this as *point gap closing*, where the spectral winding number becomes zero and signals a *spectral topological phase transition*. In higher dimensions, the eigen-energies can form spectral areas as the quasi-momenta cover the Brillouin zone (e.g. see the blue regions in Fig 5(a)). Finite spectral area and arcs with zero area, respectively, correspond to presence and absence of NH skin effect for systems with OBC [50], although direct connection with point gap topology is yet to be established [3]. However, the spec-

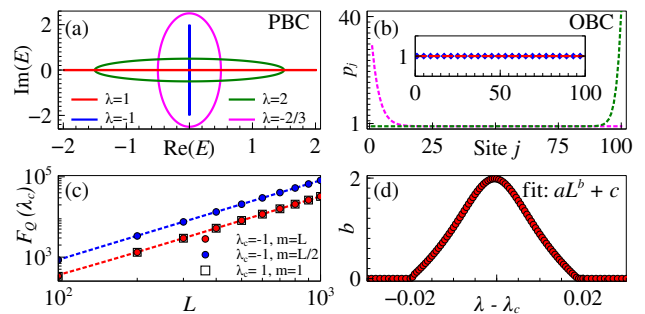


FIG. 2. Hatano-Nelson model with $\lambda = J_R/J_L$ in Eq. (1). (a) PBC spectrum. (b) Cumulative site-population for OBC eigenstates shows the NH skin effect and its absence (inset). (c) Quadratic scaling of QFI at the transition $\lambda = \lambda_c$. (d) QFI Scaling exponent near transition.

tral area can be thought to be constituted of a continuum of loops, each of which are formed by varying the momentum in only one spatial direction while keeping the other momenta fixed. Each of these loops can be associated with a spectral winding number and point gap [51]. By tuning the Hamiltonian parameters, it is possible to contract all the loops into arcs at once, which we refer to as *simultaneous point gap closing*. As a result, the total spectral area can collapse into an arc (e.g. see the red lines in Fig 5(a)), signaling a vanishing NH skin effect for any OBC geometry [50]. The other possibility, where the spectral area is nonzero but constitutes of arcs, corresponds to vanishing NH skin effect for particular OBC geometries. See Supplemental Material (SM) for more details [52]. In all such cases, changes in the nature of the OBC eigenstates can be used for sensing the parameter.

In this work, we consider first order skin effect, where almost all the eigenstates are edge-localized. When the point gap closes, all these skin states go through a sharp change and become delocalized, which makes them potential candidates for quantum-enhanced sensitivity. However, from a practical perspective, the most relevant state for evolution with a NH Hamiltonian is the right eigenstate with OBC that has the largest imaginary part in its energy as this will be the only state surviving in the long time limit [53–56]. We take this non-equilibrium steady state as the probe state for most cases considered in this work. In the following, we investigate the sensing capability of an extensive set of NH systems, with particular emphasis on the steady state, and show that point gap closing indeed results in quantum-enhanced sensitivity.

Single-band case.— We first study the Hatano-Nelson model which is a 1D chain of size L , with the Hamiltonian [57, 58]

$$H_{\text{HN}} = \sum_j (J_L |j\rangle\langle j+1| + J_R |j+1\rangle\langle j|), \quad (1)$$

where J_L and J_R are real asymmetric hopping terms towards left and right, respectively. The parameter to be estimated is $\lambda = J_R/J_L$. At $\lambda = \lambda_c = \pm 1$ the system's point gap closes, signalled by a change in the winding number (see SM [52]). Note that while at $\lambda_c = 1$ the Hamiltonian becomes Hermitian, $\lambda_c = -1$ makes it anti-Hermitian. Under PBC, this Hamiltonian

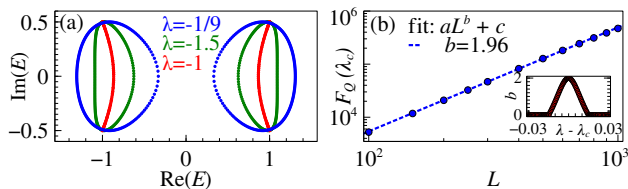


FIG. 3. Non-Hermitian SSH model with $\lambda = J_{1R}/J_{1L}$ in Eq. (3). Here $J_2=1$. (a) PBC spectrum. (b) Quadratic scaling of QFI at the transition. (Inset) QFI Scaling exponent near transition.

can be diagonalized in the quasi-momentum $|k\rangle$ basis, with a single-band spectrum $E_k=(J_L+J_R)\cos k+i(J_L-J_R)\sin k$, with $k\in[0,2\pi)$. In Fig. 2(a), we plot this spectrum in the complex energy plane which forms closed loops for $\lambda\neq\lambda_c$. Point gap closing occurs at the critical values $\lambda=\lambda_c$, for which the loops contract to a line. The spectrum changes dramatically if one considers OBC instead. Here the analytical solutions can be obtained by employing the generalized Brillouin zone (GBZ) formalism where the translational invariance in the large system size limit is exploited to write down an ansatz for a bulk eigenstate as $|\psi\rangle=\sum_j\beta^j\phi|j\rangle$ [47, 59–61]. For the Hatano-Nelson model, there are two solutions for β satisfying $|\beta|=\sqrt{|\lambda|}$. The energies are given by $E_m=2(J_RJ_L)^{1/2}\cos\frac{m\pi}{L+1}$, with $m\in[1, L]$, and the corresponding eigenstates are $|E_m\rangle=\sum_j w_{j,m}|j\rangle$ in which [52, 60, 62]

$$w_{j,m} = \mathcal{N}_m \lambda^{j/2} \sin \frac{m\pi}{L+1}, \quad (2)$$

with the normalization factor \mathcal{N}_m . Due to the presence of $\lambda^{j/2}$ in Eq. (2), for $\lambda\neq\lambda_c$, every eigenstate is exponentially localized at either edge with localization length $\sim 1/\log(|\lambda|)$. In contrast, the eigenstates become delocalized at λ_c and equivalently $|\beta|\rightarrow 1$. To see this more explicitly one can define the cumulative population at site j as $p_j=\sum_m |w_{j,m}|^2$ which is displayed in Fig. 2(b), for the same λ values as in Fig. 2(a). The localization of p_j clearly shows that whenever the PBC spectrum forms a loop, all the corresponding OBC eigenstates localize at the edges, which is the NH skin effect. To evaluate how the sensitivity scales with the system size, we compute the QFI with respect to λ for different OBC eigenstates. In Fig. 2(c), the QFI at the transition $F_Q(\lambda_c)$ is plotted for the three representative eigenstates indexed by $m=1, 2, L$. The scaling at the transition $F_Q(\lambda_c)\sim aL^b$, with $b\approx 2$, clearly shows critically-enhanced Heisenberg scaling for all eigenstates. The analytical derivation of this scaling is presented in the SM [52]. Unlike exponent b , coefficient a depends on the choice of the eigenstate. To study the sensitivity across the transition, in Fig. 2(d) we plot the exponent b versus $\lambda-\lambda_c$ with $\lambda_c=-1$ for the eigenstate with $m=L$, corresponding to the largest imaginary energy. Other eigenstates behave similarly. Deviation from the transition causes the exponent b to eventually vanish, signaling the emergence of a localized phase.

Two-band case.— Our next focus is the NH extension of the Su–Schrieffer–Heeger (SSH) model for an 1D chain with L

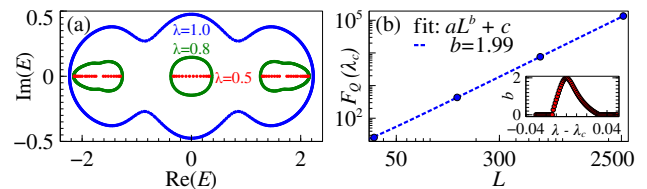


FIG. 4. Non-Hermitian AAH model with $\lambda = h$ in Eq. (4). Here $J=V=1$, $\alpha=(\sqrt{5}+1)/2$, $\theta=0$. (a) PBC spectrum. (b) Quadratic scaling of QFI at the transition. (Inset) QFI Scaling exponent near transition.

cells, each with two sites A and B [47]. The Hamiltonian is

$$H_{\text{SSH}} = \sum_j \left(J_{1L} |j, A\rangle \langle j, B| + J_{1R} |j, B\rangle \langle j, A| + J_2(|j, A\rangle \langle j+1, B| + |j+1, B\rangle \langle j, A|) \right), \quad (3)$$

with asymmetric intra-cell hoppings J_{1L} and J_{1R} and inter-cell hopping J_2 . The parameter of interest is $\lambda=J_{1R}/J_{1L}$. Here, due to the presence of two sub-lattices (A and B), the PBC spectrum generally forms two loops in the complex energy plane (similarly to two bands in the Hermitian case). Consequently, this model shows a rich phase diagram as a function of the Hamiltonian parameters. This includes: (i) merging of two loops into a single one, signaling line gap closing, equivalent to the standard Hermitian band gap closing; and (ii) shrinking of loops into arcs (as in the previous model), signaling point gap closing (red curve in Fig. 3(a)). As before, the presence of the PBC spectral loops correspond to localized OBC bulk states, namely NH skin effect. The GBZ ansatz here results again in two possible localization parameters satisfying $|\beta|=\sqrt{|\lambda|}$ [62], see the SM [52] for more details. In Fig. 3(a), we set $J_2=1$ and plot the PBC spectrum for different values of λ . The spectral loops collapse into arcs when $|\lambda|=1$, where the point gap closes and the OBC eigenstates delocalize as $|\beta|\rightarrow 1$. To investigate the sensitivity at the transition, we calculate the QFI of the OBC eigenstate with largest imaginary energy (i.e. the steady state) at $\lambda_c=-1$. There are two eigenstates with largest imaginary energy near λ_c , with equal and opposite real energies. We have numerically checked that the QFI at the transition behaves similarly for both the states as well as for their superpositions. In Fig. 3(b), the QFI is plotted against the system size L for the state with largest imaginary energy and negative real energy. Again one observes the critically-enhanced Heisenberg scaling $F_Q(\lambda_c)\sim L^b$, with $b\approx 2$. As the inset shows, the enhancement decreases away from λ_c . Note that the enhanced sensitivity is generic to all eigenstates and the choice of this specific eigenstate is motivated by its dominance in the long-time dynamics.

Disordered case.— We now consider a NH version of the Aubrey-André-Harper (AAH) Hamiltonian, given by [63]

$$H_{\text{AAH}} = \sum_j \left(J(|j\rangle \langle j+1| + \text{h.c.}) + V \cos(2\pi\alpha j + \theta + ih) |j\rangle \langle j| \right). \quad (4)$$

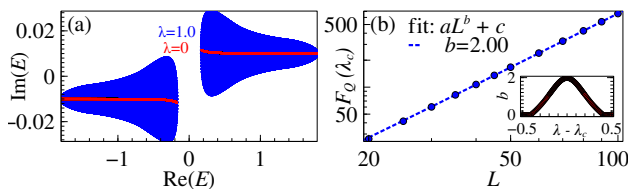


FIG. 5. Non-Hermitian QWZ model with $\lambda = t_1/m_z$ in Eq. (5). (a) PBC spectrum. The fixed parameters for a $L \times L$ lattice are, $m_z=1, t_2=0.2, \gamma_x=0.1, \gamma_y=0.1, \gamma_z=0.01, L=200$. (b) Quadratic scaling of QFI at the transition for OBC along both directions. (Inset) QFI Scaling exponent near the transition for the same OBC.

Here J is a standard hopping parameter, while V is the disorder amplitude, α the (irrational) quasi-frequency, θ a real phase and h is the strength of an imaginary phase which has to be estimated. The value $h_c = \log(2J/V)$ is a multi-critical point for both parity-time (PT) symmetry breaking and localization transitions, captured by a spectral winding number with θ running from 0 to 2π (see SM [52] for more details). In the thermodynamic limit, this number vanishes for $h < h_c$ while the eigenstates are delocalized with real PBC spectrum (unbroken PT phase). For $h > h_c$, instead, the winding number is -1 and the eigenstates are now localized with complex PBC spectrum (broken PT phase) that can form spectral loops (see Fig. 4(a)). Due to lack of translational invariance, the GBZ formalism does not apply here. To avoid finite-size effects, we follow the standard numerical procedure [64, 65] for choosing the irrational parameter α . Accordingly, for a system size $L = \mathcal{F}_n$ (with \mathcal{F}_n as the n -th Fibonacci number), α is approximated by $\mathcal{F}_{n+1}/\mathcal{F}_n$. As $n \rightarrow \infty$, α converges to the golden ratio $(\sqrt{5}+1)/2$. To infer the scaling of the QFI with respect to h (i.e. for $\lambda=h, \lambda_c=h_c$) versus system size, we vary n between 9 (corresponding to $L=34$) and 18 (corresponding to $L=2584$). In Fig. 4(b) we plot $F_Q(\lambda_c)$ as a function of L , which again shows Heisenberg scaling $F_Q(\lambda_c) \sim L^b$, with $b \approx 2$. This scaling is in agreement with that of the fidelity susceptibility in the Hermitian case [65]. In the inset we show the behavior of b away from the transition. The above results also show the robustness of sensors based on topological systems against local perturbations, as the Hatano-Nelson model with random disorder can be mapped to the Hamiltonian H_{AAH} [63].

Two-dimensional case.— As a prototypical 2D topological model, we consider a NH version of the Qi-Wu-Zhang (QWZ) Chern insulator [59, 66, 67]. This is a bipartite square lattice with Bloch Hamiltonian at momentum $\mathbf{k} = (k_x, k_y)$ given by

$$H_{QWZ}(\mathbf{k}) = (2t_1 \sin k_x + i\gamma_x)\sigma_x + (2t_1 \sin k_y + i\gamma_y)\sigma_y + [m_z - 2t_2(\cos k_x + \cos k_y) + i\gamma_z]\sigma_z, \quad (5)$$

where $\sigma_{x,y,z}$ are the Pauli matrices, t_1, t_2 are hopping parameters, m_z is an onsite term (which is fixed to unity), and $\gamma_{x,y,z}$ are the imaginary terms making the system NH. We note that, since there is no unique definition of spectral winding number in 2D systems, requiring the value of the critical parameter for the transition requires some care. We now briefly outline how

to determine the parameters driving the transition (see SM for further details [52]). The PBC spectrum generically consists of two spectral areas corresponding to two bands, shown as blue areas in Fig. 5(a). Each band in turn can be decomposed into spectral loops each forming when k_y (for example) varies in the first Brillouin zone, while k_x is held fixed. Accordingly, a k_x -dependent spectral winding number can be written for each loop relying on their point gap topology. The parameter values for the transition are then found using the same GBZ formalism as in 1D models. The simultaneous point gap closing occurs at three independent points, $t_1/m_z=0, t_2/m_z=0$, and $\gamma_y/m_z=0$ (the other Hamiltonian parameters being fixed to arbitrary values). Further numerical inspection reveals that only at $t_1/m_z=0$, the contractions happen in such a way that they collectively also form an overall arc for the PBC spectrum (see red curve in Fig. 5(a)). Hence, the collapse of the spectral area corresponds to vanishing NH skin effect for any OBC geometry [50]. Choosing $\lambda=t_1/m_z$ with $\lambda_c=0$ and OBC along both directions, we calculate the QFI for the OBC eigenstate with largest imaginary energy (i.e. the steady state). For an $L \times L$ lattice, we find the scaling of QFI at transition as $F_Q(\lambda_c) \sim L^b$, with $b \approx 2$. The inset shows how b decreases away from λ_c . The other simultaneous point gap closing instances correspond to vanishing of skin effect if OBC is only along y , and similar scaling of QFI is found for that OBC geometry.

Optimal measurement basis.— These prototypical examples regarding the NH spectral topology establish the connection between point gap closing and quantum-enhanced sensing with the physically relevant states. It turns out that the optimal measurement basis is given by the position basis (except for the disordered case where $\sim 95\%$ of QFI is obtained). This is local in nature, hence easily implementable in practice.

Experimental realization.— NH models with skin effects are routinely realized in various experimental platforms such as, electric circuits [68–70], acoustic [71, 72] and photonic lattices [73, 74], and mechanical metamaterials [75, 76]. In the context of quantum simulations, the NH version of SSH model has been realized with lossy optical lattices [77, 78]. An excellent candidate for probing the point gap closing is the photonic discrete-time quantum walk experiment where the NH skin effect has been observed [79–82]. The non-Unitary evolution of the walker consists of rotations of photon polarization and corresponding shifts along the lattice where the non-Hermiticity is implemented by a gain-loss operation at each site. The point gap closing location can be found with the GBZ formalism as before [80]. Therefore, by tuning the experimental parameters, specifically the polarization rotation close to the transition, it should be possible to probe the findings reported in this work. Moreover, the measurements in such experiments are carried out in the position basis, which is the optimal basis as discussed above.

Conclusion.— In this work, through investigation of several paradigmatic NH topological systems, we showed that quantum-enhanced sensitivity for the bulk Hamiltonian parameters can be achieved with Heisenberg scaling. In particular, we found that the origin of such enhanced precision is

tightly connected with the closing of point gaps which affects the entire spectrum. Remarkably, this kind of gap closing is a genuinely NH phenomenon with no analogue in Hermitian physics. We point out that realizing NH Hamiltonians require *open* quantum systems. In this respect, our work shows that, despite being usually detrimental to sensing, decoherence can be a resource for quantum-enhanced sensitivity, thus offering practical advantages. Finally, we showed potential implementations of our protocol in various experimental platforms.

F. C. and A. C. acknowledge support from University of Palermo through project “Bando Eurostart 2022”. A. B. acknowledges support from the National Key R&D Program of China (Grant No. 2018YFA0306703), National Science Foundation of China (Grants No. 12050410253 and No. 92065115) and the Ministry of Science and Technology of China (Grant No. QNJ2021167001L).

* saubhik.sarkar@uestc.edu.cn

† francesco.ciccarello@unipa.it

‡ angelo.carollo@unipa.it

§ abolfazl.bayat@uestc.edu.cn

- [1] Y. Ashida, Z. Gong, and M. Ueda, *Advances in Physics* **69**, 249 (2020).
- [2] E. J. Bergholtz, J. C. Budich, and F. K. Kunst, *Rev. Mod. Phys.* **93**, 015005 (2021).
- [3] N. Okuma and M. Sato, *Annual Review of Condensed Matter Physics* **14**, 83 (2023).
- [4] K. Kawabata, K. Shiozaki, M. Ueda, and M. Sato, *Phys. Rev. X* **9**, 041015 (2019).
- [5] J. Wiersig, *Phys. Rev. Lett.* **112**, 203901 (2014).
- [6] Z.-P. Liu, J. Zhang, i. m. c. K. Özdemir, B. Peng, H. Jing, X.-Y. Lü, C.-W. Li, L. Yang, F. Nori, and Y.-x. Liu, *Phys. Rev. Lett.* **117**, 110802 (2016).
- [7] W. Langbein, *Phys. Rev. A* **98**, 023805 (2018).
- [8] H.-K. Lau and A. A. Clerk, *Nature Communications* **9**, 4320 (2018).
- [9] M. Zhang, W. Sweeney, C. W. Hsu, L. Yang, A. D. Stone, and L. Jiang, *Phys. Rev. Lett.* **123**, 180501 (2019).
- [10] C. Chen, L. Jin, and R.-B. Liu, *New Journal of Physics* **21**, 083002 (2019).
- [11] J. C. Budich and E. J. Bergholtz, *Phys. Rev. Lett.* **125**, 180403 (2020).
- [12] F. Koch and J. C. Budich, *Phys. Rev. Research* **4**, 013113 (2022).
- [13] H. Schomerus, *Phys. Rev. Research* **2**, 013058 (2020).
- [14] A. McDonald and A. A. Clerk, *Nature Communications* **11**, 5382 (2020).
- [15] H. Hodaei, A. U. Hassan, S. Wittek, H. Garcia-Gracia, R. El-Ganainy, D. N. Christodoulides, and M. Khajavikhan, *Nature* **548**, 187 (2017).
- [16] S. Yu, Y. Meng, J.-S. Tang, X.-Y. Xu, Y.-T. Wang, P. Yin, Z.-J. Ke, W. Liu, Z.-P. Li, Y.-Z. Yang, G. Chen, Y.-J. Han, C.-F. Li, and G.-C. Guo, *Phys. Rev. Lett.* **125**, 240506 (2020).
- [17] H. Wang, Y.-H. Lai, Z. Yuan, M.-G. Suh, and K. Vahala, *Nature Communications* **11**, 1610 (2020).
- [18] E. Edvardsson and E. Ardonne, *Phys. Rev. B* **106**, 115107 (2022).
- [19] W. Ding, X. Wang, and S. Chen, *Phys. Rev. Lett.* **131**, 160801 (2023).
- [20] M. G. Paris, *Int. J. Quantum Inf.* **07**, 125 (2009).
- [21] V. Giovannetti, S. Lloyd, and L. Maccone, *Science* **306**, 1330 (2004).
- [22] V. Giovannetti, S. Lloyd, and L. Maccone, *Phys. Rev. Lett.* **96**, 010401 (2006).
- [23] F. Fröwis and W. Dür, *Phys. Rev. Lett.* **106**, 110402 (2011).
- [24] K. Wang, X. Wang, X. Zhan, Z. Bian, J. Li, B. C. Sanders, and P. Xue, *Phys. Rev. A* **97**, 042112 (2018).
- [25] H. Kwon, K. C. Tan, T. Volkoff, and H. Jeong, *Phys. Rev. Lett.* **122**, 040503 (2019).
- [26] R. Demkowicz-Dobrzański, J. Kołodyński, and M. Guţă, *Nat. Commun.* **3**, 1063 (2012).
- [27] A. De Pasquale, D. Rossini, P. Facchi, and V. Giovannetti, *Phys. Rev. A* **88**, 052117 (2013).
- [28] P. Zanardi and N. Paunković, *Phys. Rev. E* **74**, 031123 (2006).
- [29] P. Zanardi, H. Quan, X. Wang, and C. Sun, *Phys. Rev. A* **75**, 032109 (2007).
- [30] P. Zanardi, M. G. Paris, and L. C. Venuti, *Phys. Rev. A* **78**, 042105 (2008).
- [31] C. Invernizzi, M. Korbman, L. C. Venuti, and M. G. Paris, *Phys. Rev. A* **78**, 042106 (2008).
- [32] S.-J. Gu, *Int. J. Mod. Phys. B* **24**, 4371 (2010).
- [33] S. Gammelmark and K. Mølmer, *New J. Phys.* **13**, 053035 (2011).
- [34] M. Skotiniotis, P. Sekatski, and W. Dür, *New J. Phys.* **17**, 073032 (2015).
- [35] M. M. Rams, P. Sierant, O. Dutta, P. Horodecki, and J. Zakrzewski, *Phys. Rev. X* **8**, 021022 (2018).
- [36] Y. Chu, S. Zhang, B. Yu, and J. Cai, *Phys. Rev. Lett.* **126**, 010502 (2021).
- [37] R. Liu, Y. Chen, M. Jiang, X. Yang, Z. Wu, Y. Li, H. Yuan, X. Peng, and J. Du, *npj Quantum Inf.* **7**, 1 (2021).
- [38] V. Montenegro, U. Mishra, and A. Bayat, *Phys. Rev. Lett.* **126**, 200501 (2021).
- [39] U. Mishra and A. Bayat, *Phys. Rev. Lett.* **127**, 080504 (2021).
- [40] U. Mishra and A. Bayat, *Scientific Reports* **12**, 14760 (2022).
- [41] X. He, R. Yousefjani, and A. Bayat, *Phys. Rev. Lett.* **131**, 010801 (2023).
- [42] R. Yousefjani, X. He, and A. Bayat, *Chinese Physics B* **32**, 100313 (2023).
- [43] V. Montenegro, M. G. Genoni, A. Bayat, and M. G. A. Paris, *Communications Physics* **6**, 304 (2023).
- [44] F. Iemini, R. Fazio, and A. Sanpera, *arXiv:2306.03927* (2023).
- [45] S. Sarkar, C. Mukhopadhyay, A. Alase, and A. Bayat, *Phys. Rev. Lett.* **129**, 090503 (2022).
- [46] M. Z. Hasan and C. L. Kane, *Rev. Mod. Phys.* **82**, 3045 (2010).
- [47] S. Yao and Z. Wang, *Phys. Rev. Lett.* **121**, 086803 (2018).
- [48] N. Okuma, K. Kawabata, K. Shiozaki, and M. Sato, *Phys. Rev. Lett.* **124**, 086801 (2020).
- [49] K. Zhang, Z. Yang, and C. Fang, *Phys. Rev. Lett.* **125**, 126402 (2020).
- [50] K. Zhang, Z. Yang, and C. Fang, *Nature Communications* **13**, 2496 (2022).
- [51] J. Zhong, K. Wang, Y. Park, V. Asadchy, C. C. Wojcik, A. Dutt, and S. Fan, *Phys. Rev. B* **104**, 125416 (2021).
- [52] See Supplemental Material for further details.
- [53] Z. Gong, Y. Ashida, K. Kawabata, K. Takasan, S. Higashikawa, and M. Ueda, *Phys. Rev. X* **8**, 031079 (2018).
- [54] S. Lieu, *Phys. Rev. B* **100**, 085110 (2019).
- [55] A. Panda and S. Banerjee, *Phys. Rev. B* **101**, 184201 (2020).
- [56] A. Banerjee, S. S. Hegde, A. Agarwala, and A. Narayan, *Phys. Rev. B* **105**, 205403 (2022).
- [57] N. Hatano and D. R. Nelson, *Phys. Rev. Lett.* **77**, 570 (1996).

- [58] N. Hatano and D. R. Nelson, *Phys. Rev. B* **56**, 8651 (1997).
- [59] S. Yao, F. Song, and Z. Wang, *Phys. Rev. Lett.* **121**, 136802 (2018).
- [60] K. Yokomizo and S. Murakami, *Phys. Rev. Lett.* **123**, 066404 (2019).
- [61] K. Yokomizo and S. Murakami, *Phys. Rev. B* **107**, 195112 (2023).
- [62] C.-X. Guo, C.-H. Liu, X.-M. Zhao, Y. Liu, and S. Chen, *Phys. Rev. Lett.* **127**, 116801 (2021).
- [63] S. Longhi, *Phys. Rev. Lett.* **122**, 237601 (2019).
- [64] H. Jiang, L.-J. Lang, C. Yang, S.-L. Zhu, and S. Chen, *Phys. Rev. B* **100**, 054301 (2019).
- [65] B.-B. Wei, *Phys. Rev. A* **99**, 042117 (2019).
- [66] H. Shen, B. Zhen, and L. Fu, *Phys. Rev. Lett.* **120**, 146402 (2018).
- [67] X.-L. Qi, Y.-S. Wu, and S.-C. Zhang, *Phys. Rev. B* **74**, 085308 (2006).
- [68] T. Helbig, T. Hofmann, S. Imhof, M. Abdelghany, T. Kiessling, L. W. Molenkamp, C. H. Lee, A. Szameit, M. Greiter, and R. Thomale, *Nature Physics* **16**, 747 (2020).
- [69] T. Hofmann, T. Helbig, F. Schindler, N. Salgo, M. Brzezińska, M. Greiter, T. Kiessling, D. Wolf, A. Vollhardt, A. Kabaši, C. H. Lee, A. Bilušić, R. Thomale, and T. Neupert, *Phys. Rev. Res.* **2**, 023265 (2020).
- [70] S. Liu, R. Shao, S. Ma, L. Zhang, O. You, H. Wu, Y. J. Xiang, T. J. Cui, and S. Zhang, *Research* **2021** (2021), 10.34133/2021/5608038.
- [71] L. Zhang, Y. Yang, Y. Ge, Y.-J. Guan, Q. Chen, Q. Yan, F. Chen, R. Xi, Y. Li, D. Jia, S.-Q. Yuan, H.-X. Sun, H. Chen, and B. Zhang, *Nature Communications* **12**, 6297 (2021).
- [72] H. Gao, H. Xue, Z. Gu, L. Li, W. Zhu, Z. Su, J. Zhu, B. Zhang, and Y. D. Chong, *Phys. Rev. B* **106**, 134112 (2022).
- [73] S. Weidemann, M. Kremer, T. Helbig, T. Hofmann, A. Stegmaier, M. Greiter, R. Thomale, and A. Szameit, *Science* **368**, 311 (2020).
- [74] Y. Song, W. Liu, L. Zheng, Y. Zhang, B. Wang, and P. Lu, *Phys. Rev. Appl.* **14**, 064076 (2020).
- [75] M. Brandenbourger, X. Locsin, E. Lerner, and C. Coulais, *Nature Communications* **10**, 4608 (2019).
- [76] A. Ghatak, M. Brandenbourger, J. van Wezel, and C. Coulais, *Proceedings of the National Academy of Sciences* **117**, 29561 (2020).
- [77] S. Lapp, J. Ang'ong'a, F. A. An, and B. Gadway, *New Journal of Physics* **21**, 045006 (2019).
- [78] W. Gou, T. Chen, D. Xie, T. Xiao, T.-S. Deng, B. Gadway, W. Yi, and B. Yan, *Phys. Rev. Lett.* **124**, 070402 (2020).
- [79] L. Xiao, T. Deng, K. Wang, G. Zhu, Z. Wang, W. Yi, and P. Xue, *Nature Physics* **16**, 761 (2020).
- [80] L. Xiao, T. Deng, K. Wang, Z. Wang, W. Yi, and P. Xue, *Phys. Rev. Lett.* **126**, 230402 (2021).
- [81] Q. Lin, T. Li, L. Xiao, K. Wang, W. Yi, and P. Xue, *Nature Communications* **13**, 3229 (2022).
- [82] Q. Lin, T. Li, L. Xiao, K. Wang, W. Yi, and P. Xue, *Phys. Rev. Lett.* **129**, 113601 (2022).

SUPPLEMENTAL MATERIAL: Quantum-enhanced sensing from non-Hermitian topology

Saubhik Sarkar,¹ Francesco Ciccarello,^{2,3} Angelo Carollo,² and Abolfazl Bayat^{1,4}

¹*Institute of Fundamental and Frontier Sciences, University of Electronic Science and Technology of China, Chengdu 610051, China*

²*Università degli Studi di Palermo, Dipartimento di Fisica e Chimica – Emilio Segrè, via Archirafi 36, I-90123 Palermo, Italy*

³*NEST, Istituto Nanoscienze-CNR, Piazza S. Silvestro 12, 56127 Pisa, Italy,*

⁴*Key Laboratory of Quantum Physics and Photonic Quantum Information, Ministry of Education, University of Electronic Science and Technology of China, Chengdu 611731, China*

Spectral winding number

Non-Hermitian Hamiltonians have complex eigen-energies which gives rise to an unique spectral topology that has no correspondence in Hermitian systems. The topological invariant is determined by the winding of the phase of the complex energies. This is given by the spectral winding number. In 1D lattices with translational invariance, it is defined, with respect to a reference energy E_0 , as

$$w_{1D}(E_0) = \frac{1}{2\pi i} \int_0^{2\pi} dk \partial_k \ln(E_k - E_0). \quad (\text{S1})$$

Spectral winding number in a 2D system for winding along y -direction for a given value of momentum along x -direction with respect to a reference energy E_0 is defined as

$$w_{2D}(k_x, E_0) = \frac{1}{2\pi i} \int_0^{2\pi} dk_y \partial_{k_y} \ln(E_k - E_0). \quad (\text{S2})$$

For the (quasi) disordered model in Eq. (4), the winding number is defined by circulating the real phase θ of the disorder potential from 0 to 2π while taking the thermodynamic limit, i.e. system size $L \rightarrow \infty$. Keeping the other parameter fixed, the Hamiltonian can be considered as a function of the phase, i.e. $H_{AAH}(\theta)$, and the winding number with respect to a reference energy E_0 is

$$w_{AAH}(E_0) = \frac{1}{2\pi i} \int_0^{2\pi} d\theta \partial_\theta \ln \det(H_{AAH}(\theta) - E_0). \quad (\text{S3})$$

Hatano-Nelson model

Hatano-Nelson model is a single-band model that captures the uniqueness of NH topology due to asymmetric hopping parameters to left and right on an 1D chain. The Hamiltonian is given by the Eq. (1) in the main text. The model is schematically depicted in Fig. S1(a). The winding number in Eq. (S1) takes values 1 and -1 for $|J_R/J_L| < 1$ and $|J_R/J_L| > 1$, respectively. The ansatz for a bulk eigenstate within the GBZ formalism in the presence of NH skin effect for OBC is

$$|\psi\rangle = \sum_j \beta^j \phi |j\rangle. \quad (\text{S4})$$

The eigen-equation $H_{HN} |\psi\rangle = E |\psi\rangle$ in the bulk gives

$$J_L \beta^2 - E\beta + J_R = 0. \quad (\text{S5})$$

The two solutions β_1 and β_2 satisfy, with definition $\lambda \equiv J_R/J_L \equiv z^2 = (re^{i\theta})^2$,

$$\beta_1 \beta_2 = \frac{J_R}{J_L} = r^2 e^{i2\theta} \quad \text{and} \quad \beta_1 + \beta_2 = \frac{E}{J_L}. \quad (\text{S6})$$

The full solution is the superposition

$$|\psi\rangle = \sum_j (c_1 \beta_1^j \phi_1 + c_2 \beta_2^j \phi_2) |j\rangle. \quad (\text{S7})$$

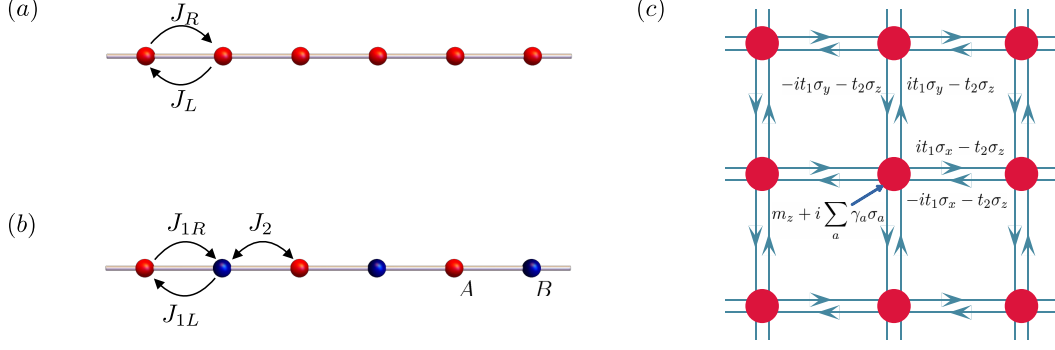


FIG. S1. Schematics of some of the NH models considered in this work. (a) HN model. (b) NH version of SSH model. (c) NH version of 2D Chern insulator based on QWZ model.

Using it for the eigen-equation at the boundaries ($j = 1, L$) and using Eq. (S6) result in $\phi_1 = -\phi_2$ and

$$\left(\frac{\beta_1}{\beta_2}\right)^{L+1} = 1 \implies \frac{\beta_1}{\beta_2} = e^{i2\theta_m}, \quad (\text{S8})$$

where $\theta_m = m\pi/(L+1)$ with $m \in [1, L]$, as $m = L+1$ corresponds to the trivial solution. Therefore we have $|\beta_1| = |\beta_2| = r$. Choosing $\beta_1 = re^{i\theta^{(1)}}$, $\beta_2 = re^{i\theta^{(2)}}$ and solving $\theta^{(1)} + \theta^{(2)} = 2\theta_m$ and $\theta^{(1)} - \theta^{(2)} = 2\theta$ gives us the solution presented in the main text

$$\begin{aligned} |\psi_m\rangle &= \mathcal{N}_m \sum_j \lambda^{\frac{j}{2}} \sin \frac{m\pi}{L+1} = \mathcal{N}_m \sum_j r^j e^{ij\theta} \frac{\omega_m - \omega_m^{-1}}{2i}, \quad \text{with} \\ \omega_m &= e^{\frac{im\pi}{L+1}}, \quad \text{and} \\ \mathcal{N}_m &= \frac{2}{\sqrt{2 \frac{1-|\lambda|^L}{1-|\lambda|} - \frac{1-|\lambda|^L e^{i\frac{2m\pi L}{L+1}}}{1-|\lambda|e^{i\frac{2m\pi}{L+1}}} - \frac{1-|\lambda|^L e^{-i\frac{2m\pi L}{L+1}}}{1-|\lambda|e^{-i\frac{2m\pi}{L+1}}}}} = \frac{2}{\sqrt{2 \frac{1-r^{2L}}{1-r^2} - \frac{1-(r\omega_m)^{2L}}{1-(r\omega_m)^2} - \frac{1-(r/\omega_m)^{2L}}{1-(r/\omega_m)^2}}}. \end{aligned} \quad (\text{S9})$$

Recalling the definition of QFI

$$F_Q(\lambda) = 4 \left(\langle \partial_\lambda \psi_m | \partial_\lambda \psi_m \rangle - |\langle \partial_\lambda \psi_m | \psi_m \rangle|^2 \right), \quad (\text{S10})$$

we first calculate $|\partial_\lambda \psi_m\rangle$. Employing the chain rule of partial differentiation with the variables (r, θ) , we write down

$$|\partial_\lambda \psi_m\rangle = (\partial_\lambda r) |\partial_r \psi_m\rangle + (\partial_\lambda \theta) |\partial_\theta \psi_m\rangle. \quad (\text{S11})$$

Now we express $|\psi_m\rangle = |\tilde{\psi}_m\rangle / \|\tilde{\psi}_m\rangle\|$, with $|\tilde{\psi}_m\rangle = \sum_j (re^{i\theta})^j \sin(m\pi/(L+1)) |j\rangle$, and observe that $|\partial_\theta \tilde{\psi}_m\rangle = ir |\partial_r \tilde{\psi}_m\rangle$. As $\|\tilde{\psi}_m\rangle\|$ is independent of θ , we have

$$|\partial_\theta \psi_m\rangle = \frac{1}{\|\tilde{\psi}_m\rangle\|} |\partial_\theta \tilde{\psi}_m\rangle = \frac{ir}{\|\tilde{\psi}_m\rangle\|} |\partial_r \tilde{\psi}_m\rangle = \frac{ir}{\|\tilde{\psi}_m\rangle\|} \partial_r (\|\tilde{\psi}_m\rangle\| |\psi_m\rangle) = ir \left(\partial_r |\psi_m\rangle + \frac{\partial_r \|\tilde{\psi}_m\rangle\|}{\|\tilde{\psi}_m\rangle\|} |\psi_m\rangle \right). \quad (\text{S12})$$

Inserting Eq. (S12) in Eq. (S11), we get

$$|\partial_\lambda \psi_m\rangle = (\partial_\lambda r + ir \partial_\lambda \theta) |\partial_r \psi_m\rangle + \left(ir \frac{\partial_r \|\tilde{\psi}_m\rangle\|}{\|\tilde{\psi}_m\rangle\|} \partial_\lambda \theta \right) |\psi_m\rangle \equiv a |\partial_r \psi_m\rangle + b |\psi_m\rangle. \quad (\text{S13})$$

Using Eq. (S12), the QFI can be rewritten as

$$\begin{aligned} F_Q(\lambda) &= 4|a|^2 \left(\langle \partial_r \psi_m | \partial_\lambda \psi_m \rangle - |\langle \partial_r \psi_m | \psi_m \rangle|^2 \right) \\ &= 4 \left((\partial_\lambda r)^2 + r^2 (\partial_\lambda \theta)^2 \right) \left(\langle \partial_r \psi_m | \partial_r \psi_m \rangle - |\langle \partial_r \psi_m | \psi_m \rangle|^2 \right). \end{aligned} \quad (\text{S14})$$

The pre-factor $((\partial_\lambda r)^2 + r^2(\partial_\lambda \theta)^2)$ approaches a constant value as $\lambda \rightarrow \lambda_c$, and does not depend on the system size. The L -dependence comes from derivatives with respect to r . We can write

$$\begin{aligned}
F_Q(\lambda) &= \left((\partial_\lambda r)^2 + r^2 (\partial_\lambda \theta)^2 \right) \\
&\left(2(\partial_r \mathcal{N}_m)^2 \sum_{j=1}^L \left((r)^{2j} - (r\omega)^{2j} - (r/\omega)^{2j} \right) + \frac{\mathcal{N}_m^2}{r^2} \sum_{j=1}^L j^2 \left((r)^{2j} - (r\omega)^{2j} - (r/\omega)^{2j} \right) + 4 \frac{\mathcal{N}_m \partial_r \mathcal{N}_m}{r} \sum_{j=1}^L j \left((r)^{2j} - (r\omega)^{2j} - (r/\omega)^{2j} \right) \right) \\
&- \left| 2(\mathcal{N}_m \partial_r \mathcal{N}_m) \sum_{j=1}^L \left((r)^{2j} - (r\omega)^{2j} - (r/\omega)^{2j} \right) + 2 \frac{\mathcal{N}_m^2}{r} \sum_{j=1}^L j \left((r)^{2j} - (r\omega)^{2j} - (r/\omega)^{2j} \right) \right|^2.
\end{aligned} \tag{S15}$$

As the transition, $\lambda \rightarrow \lambda_c$, and consequently, $r \rightarrow 1$. The L -dependence can be shown in the limiting values: $\mathcal{N}_m \rightarrow \sqrt{2/L}$, $\partial_r \mathcal{N}_m \rightarrow -\sqrt{L/2}$, $\sum_j (r)^{2j} \rightarrow L$, $\sum_j (r\omega_m)^{2j} \rightarrow -1$, $\sum_j (r/\omega_m)^{2j} \rightarrow -1$, $\sum_j j(r)^{2j} \rightarrow L(L+1)/2$, $\sum_j j(r\omega_m)^{2j} \rightarrow (L+1)/(\omega_m^2 - 1)$, $\sum_j j(r/\omega_m)^{2j} \rightarrow (L+1)/(\omega_m^{-2} - 1)$, $\sum_j j^2(r)^{2j} \rightarrow (2L^3 + 3L^2 + L)/6$, $\sum_j j^2(r\omega_m)^{2j} \rightarrow (L^2)/(\omega_m^2 - 1)$, $\sum_j j^2(r/\omega_m)^{2j} \rightarrow L^2/(\omega_m^{-2} - 1)$. Combining all these terms, the QFI shows L^2 scaling in large L limit.

Non-Hermitian SSH model

The NH extension of the SSH model is considered with asymmetric intra-cell hopping. The model still has sublattice symmetry. The Hamiltonian is given by the Eq. (3) in the main text. The model is schematically depicted in Fig. S1(a). The ansatz for a bulk eigenstate within the GBZ formalism in the presence of NH skin effect for OBC is

$$|\psi\rangle = \sum_j \beta^j (\phi_A |j, A\rangle + \phi_B |j, B\rangle). \tag{S16}$$

The eigen-equation $H_{\text{SSH}} |\psi\rangle = E |\psi\rangle$ in the bulk gives

$$J_2 J_{1L} \beta^2 + (J_2^2 + J_{1L} J_{1R} - E^2) \beta + J_2 J_{1R} = 0. \tag{S17}$$

The two solutions β_1 and β_2 satisfy

$$\beta_1 \beta_2 = \frac{J_{1R}}{J_{1L}} = r^2 e^{i2\theta} \quad \text{and} \quad \beta_1 + \beta_2 = \frac{E^2 - J_2^2 - J_{1L} J_{1R}}{J_2 J_{1L}}. \tag{S18}$$

The full solution is

$$|\psi\rangle = \sum_j \left((c_1 \beta_1^j \phi_{1,A} + c_2 \beta_2^j \phi_{2,A}) |j, A\rangle + (c_1 \beta_1^j \phi_{1,B} + c_2 \beta_2^j \phi_{2,B}) |j, B\rangle \right) \equiv \sum_j (\psi_{j,A} |j, A\rangle + \psi_{j,B} |j, B\rangle). \tag{S19}$$

Using it for the eigen-equation at the boundaries ($j = 1, L$) and using Eq. (S18) gives $c_1 \phi_{1,B} = -c_2 \phi_{2,B}$ and

$$\left(\frac{\beta_1}{\beta_2} \right)^{L+1} = \frac{J_{1R} + J_2 \beta_1}{J_{1R} + J_2 \beta_2}, \tag{S20}$$

with $|\beta_1| = |\beta_2| = r$. Near the transition, $J_{1R}/J_{1L} = \pm 1$. However $J_{1R} = J_{1L}$ is the Hermitian case and therefore, we focus on the $J_{1R} = -J_{1L}$ case. Here, $\beta_1 \beta_2 = -1$ and we can choose $\beta_1 = r e^{i\theta}$, $\beta_2 = -r e^{-i\theta}$. The solution for θ is given by the transcendental equation

$$\begin{aligned}
\cos(L+1)\theta + \frac{iJ_2}{\sqrt{|J_{1R}J_{1L}|}} \sin(L\theta) &= 0 \quad (\text{for even } L) \\
\sin(L+1)\theta - \frac{iJ_2}{\sqrt{|J_{1R}J_{1L}|}} \cos(L\theta) &= 0 \quad (\text{for odd } L),
\end{aligned} \tag{S21}$$

and the wavefunction is given by

$$\begin{aligned}
\psi_{j,A} &\propto (ir)^j \left(i \sin(j(\theta - \pi/2)) + \frac{J_2}{\sqrt{|J_{1R}J_{1L}|}} \cos(j(\theta - \pi/2) - \theta) \right), \\
\psi_{j,B} &\propto (ir)^j \left(\sin(j(\theta - \pi/2)) \right).
\end{aligned} \tag{S22}$$

Although we have an analytical expression for the wavefunction, it requires the knowledge of the phase θ of β . As this can only be determined by graphically solving the transcendental equations in Eq. (S21), the QFI cannot be fully expressed analytically to extract the scaling behavior. In the main text, we numerically show the quadratic scaling of QFI at the transition.

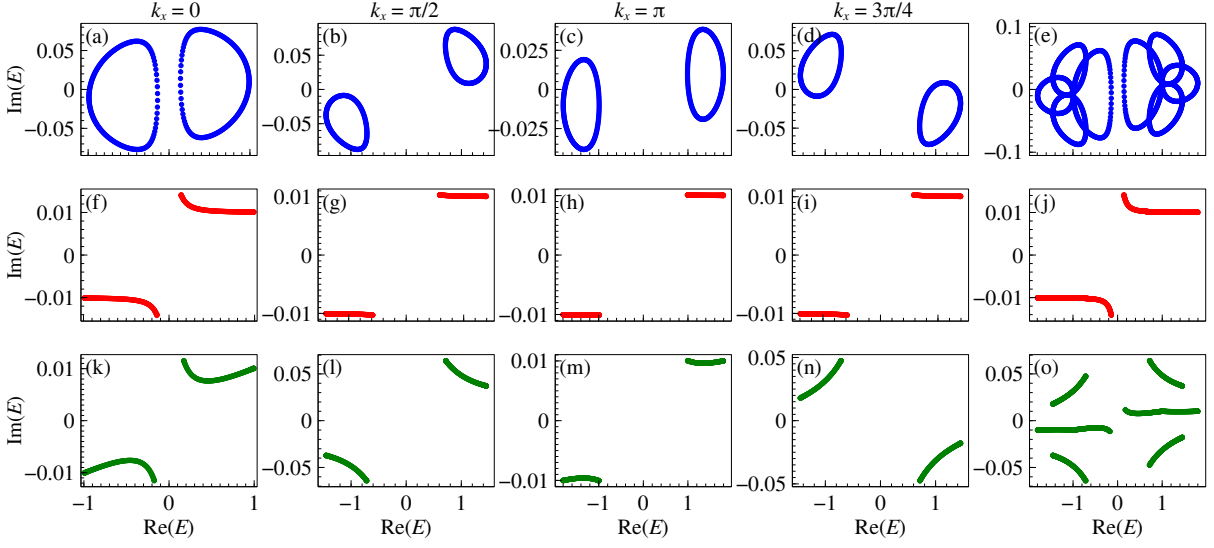


FIG. S2. Decomposition of PBC spectrum of the 2D Chern insulator model. Few k_x points are chosen to show the energy along the Brillouin zone of k_y , forming spectral loops or arcs. The fixed parameters for a 200×200 lattice are, $m_z = 1, t_2 = 0.2, \gamma_x = 0.1, \gamma_z = 0.01$. (top panel) $t_1 = 0.2, \gamma_y = 0.1$. (middle panel) $t_1 = 0, \gamma_y = 0.1$. (bottom panel) $t_1 = 0.2, \gamma_y = 0$.

Non-Hermitian 2D Chern insulator model

A NH extension of a prototypical 2D Chern insulator is considered with imaginary Zeeman terms. The Bloch Hamiltonian for a square lattice with internal levels a and b is given by the Eq. (5) in the main text. In real space the model is schematically depicted in Fig. S1(c). For this $L \times L$ lattice, the PBC spectral area can be decomposed into L number of loops in the complex energy plane, each one corresponding to a particular k_x value. This is shown for some representative k_x points in the top panel of Fig. S2 where Fig. S2(e) shows how they add up to generate the total spectral area. With suitable choice of Hamiltonian parameters, all the loops can be contracted to arcs (middle panel of Fig. S2) in such a way that the overall spectrum also has zero area, as shown in Fig. S2(j). This causes the NH skin effect to vanish irrespective of OBC geometry. The bottom panel shows another type of shrinkage to arcs which do not add up to an overall arc for the full system and the resulting spectrum still has finite area (Fig. S2(o)). In this case, NH skin effect vanishes when OBC is taken only along the y -direction. To systematically locate the critical parameters for which the two different types of NH Skin effect vanishing occur, we look at the point gap topology of a spectral loop formed at a fixed value of k_x . In this context, the ansatz for a bulk eigenstate within the GBZ formalism in the presence of NH skin effect for OBC only along y -direction is

$$|\psi\rangle = \sum_j \beta^j (\phi_a |j, a\rangle + \phi_b |j, b\rangle), \quad (\text{S23})$$

where a, b are the two internal states. The eigen-equation for the k_x -dependent quasi-1D Hamiltonian gives

$$(t_1^2 - t_2^2)\beta^4 - 2(\gamma_y t_1 + (m_z - 2t_2 \cos k_x + i\gamma_z)t_2)\beta^3 + (E^2 + \gamma_y^2 + 2(t_1^2 - t_2^2) - (m_z - 2t_2 \cos k_x + i\gamma_z)^2 - (2t_1 \sin k_x + i\gamma_x)^2)\beta^2 + 2(\gamma_y t_1 - (m_z - 2t_2 \cos k_x + i\gamma_z)t_2)\beta + (t_1^2 - t_2^2) = 0. \quad (\text{S24})$$

This is a quartic equation, but for the special case of $t_1 = t_2$, reduces to a quadratic one with the two solutions β_1 and β_2 satisfying

$$\beta_1 \beta_2 = \frac{m_z - 2t_2 \cos k_x + i\gamma_z - \gamma_y}{m_z - 2t_2 \cos k_x + i\gamma_z + \gamma_y}. \quad (\text{S25})$$

With the constraint $|\beta_1| = |\beta_2|$, it is easy to see that for $\gamma_y = 0$, the NH skin effect vanishes for the stripe geometry. This observation is in fact a known result and correspond to the bottom panel of Fig. S2. However, we numerically confirm that this also holds for $t_1 \neq t_2$. The effective 1D Hamiltonian along y -direction resembles a SSH chain with the asymmetric inter-cell hoppings $\tilde{J}_{1L} = m_z - 2t_2 \cos k_x + i\gamma_z + \gamma_y$, $\tilde{J}_{1R} = m_z - 2t_2 \cos k_x + i\gamma_z - \gamma_y$, intra-cell hopping $\tilde{J}_2 = -(t_1 + t_2)$, hopping between site a and site b in the right-adjacent cell $\tilde{J}_3 = t_1 - t_2$, and on-site gain and loss terms with strength $2t_1 \sin k_x + i\gamma_x$. For this type of SSH chain, the point gap closing occurs at $\tilde{J}_2 = \pm \tilde{J}_3$, which gives $t_1 = 0$ and $t_2 = 0$. We numerically observe that the first case correspond to the total spectral area going to zero (middle panel of Fig. S2) where as the second case is similar to that shown in the bottom panel of Fig. S2.